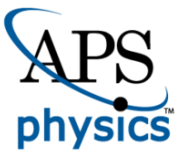

Tunneling Spectroscopy of Quantum Hall States in Bilayer Graphene p-n Junctions

Ke Wang, Achim Harzheim, Takashi Taniguchi, Kenji Watanabei, Ji Ung Lee, and Philip Kim

Phys. Rev. Lett. **122**, 146801 — Published 10 April 2019

DOI: 10.1103/PhysRevLett.122.146801

Tunneling Spectroscopy of Quantum Hall States in Bilayer Graphene PN Junctions

Ke Wang,[1,2] Achim Harzheim,[1] Takashi Taniguchi,[3] Kenji Watanabei,[3] Ji Ung Lee,[4] and Philip Kim[1]

[1] *Department of Physics, Harvard University, Cambridge, Massachusetts 02138, USA*
[2] *School of Physics and Astronomy, University of Minnesota, Minneapolis, Minnesota 55116, USA*
[3] *National Institute for Materials Science, Namiki, Ibaraki 305-0044, Japan*
[4] *College of Nanoscale Engineering and Technology Innovation, SUNY Polytechnic Institute, Albany, New York 12203, USA*

(Dated: March 11, 2019)

We report tunneling transport in spatially controlled networks of Quantum Hall (QH) edge states in bilayer graphene. By manipulating separation, location and spatial span of QH edge states via gate-defined electrostatics, we observe resonant tunneling between co-propagating QH states across incompressible strips. Employing spectroscopic tunneling measurements and an analytical model, we characterize energy gap, width, density of states, and compressibility of the QH edge states with high precision and sensitivity within the same device. The capability to engineer the QH edge network also provides an opportunity to build future quantum electronic devices with electrostatic manipulation of QH edge states, supported by rich underlying physics.

PACS numbers: 73.22.Pr, 73.43.Nq, 73.43.Fj

Two dimensional electron gases (2DEG) under strong magnetic field form quantum Hall (QH) edge states, which propagate along the sample boundary dissipationless. The quality of GaAs/AlGaAs [1, 2] and graphene [3–5] samples has significantly improved, making integer and non-Abelian fractional states resulting from exotic many-body excitations visible [6, 7]. The energy gaps and electronic compressibility of QH states have been addressed by several experimental techniques, such as single electron transistors [8, 9], optical spectroscopy [10] and capacitive measurement techniques [11]. However, while these techniques provide a direct access to the bulk properties, the spectroscopic probe of QH edge states has yet to be realized. Previously, the structure of chiral one-dimensional (1D) QH edges has been studied using scanning probe microscopy [12, 13]. The existence of conducting compressible strips (CS) separated by insulating incompressible strips (IS), has been identified near sample boundaries. For filling fraction ν in the QH regime, Landau gaps are directly related to the width of the corresponding CS and IS [14]. With electron-electron interaction, it has been shown that CS and IS can be reconstructed into fractionalized 1D modes, including the neutral charge mode [15]. In order to characterize the spatial and energetic characteristics of the QH edge states, tunneling measurement is the most ideal and sensitive tool [16]. However, in conventional quantum Hall devices, adjacent edge states tend to share the same chemical potential as the current-injecting contact, therefore the effective tunneling bias across incompressible strips vanishes. Chemical potential bias across two sets of QH states can be established using gate-defined quantum point contacts (QPC) [17]. However, the tunneling widths near QPCs are often not uniformly defined, and the QH states are without a well-defined IS region between them, obscuring the spectroscopic resolution during tunneling measurements. In this work, we report tunneling measurements in a gate-defined bilayer graphene (BLG) QH edge state network [10]. The device structure allows QH states to be uniformly spaced out and the chemical potential between them to be robustly-established. The devices consist of hBN-encapsulated graphene (mobility $\sim 30 m^{-2}/Vs$) with three local back gates and a top gate (Fig. 1A), contacted by 1D edge contacts (Fig. 1B) [18, 19]. Voltages applied to these gates electrostatically divide the sample into nine regions, determining their carrier density and the bandgap Δ. To maintain a finite tunnel barrier, we keep the sign of the displacement field unchanged across a PN junction.

Fig. 1B-C shows two different configurations of QH edge states. For each configuration, we keep the bottom two outer gates at V_E=-10 V and the top gate at V_T=+8 V, creating insulating regions in the outer middle sections (regions J2 and L2) and keeping the lead regions (region J1,J3,K1,K3,L1, and L3) P-doped. We control the transport properties of the QH edge states by changing the voltage of the bottom middle gate ΔV_B, where $\Delta V_B = 0$ is defined to be the charge neutrality point of the center region (K2). The estimated bottom gate capacitance is C = $2\text{x}10^{11} cm^{-2} V^{-1}$. We note that a change in V_B in this device scheme does not change the PN junction height, therefore it does not change the number of ISs, the width and the barrier height of each IS.

For $\Delta V_B < 0$, K2 becomes P-doped. In this unipolar gate configuration, QH edge states (filling faction ν) propagating in K2 connect the two sides of the device (Fig. 1B). For $\Delta V_B > 0$, the bridge region becomes N-doped. Consequently, the QH edge states with different carrier type are brought into close vicinity at the PN junction away from the physical edges of the device, propagating in parallel while separated by a narrow tun-

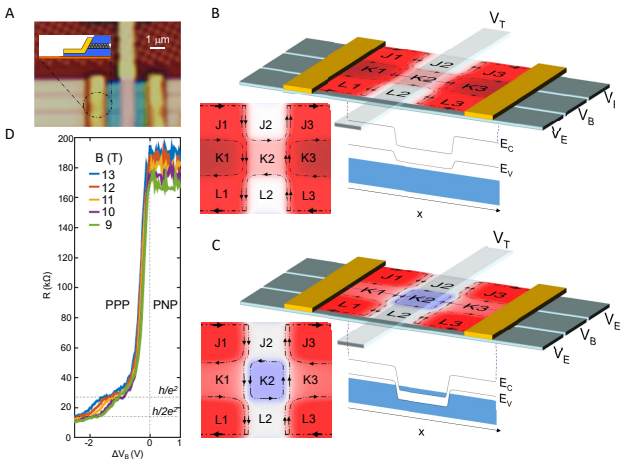

Figure 1. (Color online) Gate-defined PNP Networks in Bilayer Graphene. (A) Microscope image of the device, consisting of hBN-encapsulated bilayer graphene with three horizontal local back gates and one top gate. (inset) (B,C) Top gate V_T =8V and side back gates V_E=-10V are set to define the insulating region J2 and L2. Only the center gate V_B are swept in the experiment, and we define $\Delta V_B = 0$ at the charge neutrality point of center region K2 (V_B = -10V). Simulated carrier density and edge state configuration at (B) ΔV_B =-5V and (C) ΔV_B = 5V. The dashed lines depict the spatial distribution of edge state current under magnetic field. When $\Delta V_B < 0$ (B), current can flow through edge states whose number equals the filling factor of the center region of the device, and conventional quantum Hall transport behavior with quantized conductance plateaus is expected. However, when $\Delta V_B > 0$ (C), the N-type center region (K2) is surrounded by a finite-width insulating region with a well-defined $\nu = 0$ Landau gap and displacement-field-induced bandgap. Magneto-transport across the sample is dominated by quantum tunneling and the device enters non-equilibrium regime. (D) As a result, while quantized plateaus are clearly visible in the PPP regime (ΔV_B <0), a steep change in measured magneto resistance occurs when transitioning to the PNP regime (ΔV_B >0).

neling barrier whose height and width are set by the ν=0 QH state of the gapped BLG (Fig. 1C). We note that our experimental design brings the QH edge states into close vicinity at the PN junction allowing tunneling measurement without hot-spot formation at physical edges [20–23]. While non-equilibrium can be achieved selectively between QH edge states with different valley and spin polarization in high quality PN junction devices [21, 24], our device architecture ensures non-equilibrium chemical potential distribution between all QH edge states by spatially separating them (see SI).

The different QH edge state configurations result in distinctly different magneto-transport across the device. Fig. 1D shows a two-terminal resistance as a function of ΔV_B for several different fixed magnetic fields. As the sign of ΔV_B changes from negative to positive, the channel configuration turns from PPP into PNP. In the PPP configuration, we find well-defined plateaus corresponding to ν =1 and 2 in K2. As ΔV_B increases, the channel resistance increases steeply. In particular, across the PPP-PNP boundary (ΔV_B=0), the resistance increases more than ten-fold, indicating tunneling transport across a barrier.

We investigate the transition regime further in Fig. 2A by plotting the conductance and resistance as a function of ΔV_B and magnetic field B. In the unipolar regime ($\Delta V_B < 0$), we observe a series of QH plateaus, at a relatively low field of 2 T, corresponding to filling factions ν =1, 2, 3, 4, and 5. In the bipolar regime ($\Delta V_B > 0$), however, there is no observable quantized conductance. Instead, the transport in the device shows two distinct features: (i) In the low field regime $B < B_C \sim$ 4.5 T, the resistance increases slowly. This is followed by a rapid increase of resistance for $B > B_C$. (ii) Near the critical field, we observe resistance oscillations that are approximately independent of ΔV_B. These two features are closely related to the onset of tunneling across QH edge states, as we discuss in detail below.

For $B < B_c$, the magnetic length $l_B = \sqrt{\frac{\hbar}{eB}}$ is longer than the tunneling barrier width d_{IS} set by the $\nu \neq 0$ incompressible strips (Fig. 2D). Since the decay length of the Landau level (LL) wave function across the IS is on the order of l_B, the QH edge states along the PN boundaries tend to be highly equilibrated [13]. The total resistance across the PNP junction is the sum of the QH resistances of each doped region: $R = -\frac{2h}{\nu e^2} + \frac{h}{\nu' e^2}$, where ν' and ν are the filling fraction of the N and P regions, respectively. Note that ν' is positive and ν is negative by definition. Similar transport was observed previously [22, 23], where full/partial equilibration occurred across the PN junction. Fig. 2B shows measured resistance (R), expected resistance with full equilibrium (R_e), fitting of the low field data using our analytical quantum tunneling model in semiclassical regime (R_S) and their ratio (R/R_e) as a function of magnet field sweep at ΔV_B =5V (equal carrier density for P and N region, corresponding to the white dashed line in Fig. 2A). In the low field regime ($B < B_C$), we observe that $R \approx R_e$ as expected. However, as B approaches B_C, $R(B)$ starts to deviate from Re. For $B > B_C$, R increases exponentially as shown in Fig. 2B, and tunneling transport between well separated QH edges dominates (Fig. 2E).

Further quantitative analysis can be made by considering the tunneling process between QH edge states across ISs of the width d_{IS}. The current in each QH edge state is carried by a compressible electronic state with spatially varying chemical potential $eV_N(y)$, where y is the position along the direction of the PN junction and N is the index for the QH edge states. We consider successive tunneling between neighboring QH edge states. Current conservation in a small length dy of the Nth QH edge

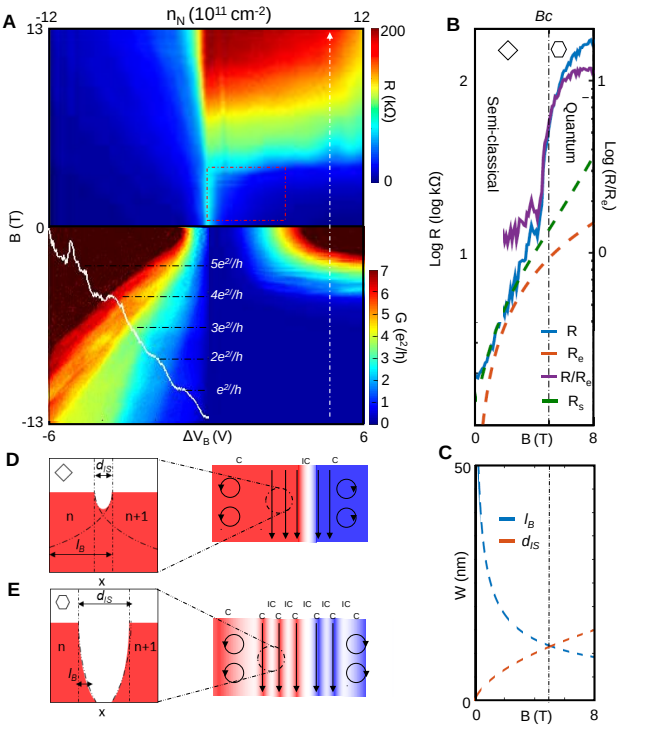

Figure 2. (Color online) Quantum Hall Phase Transition in PN Configuration. (A) Measured (top panel) resistance and (bottom panel) conductance across the device as a function of magnetic field B and central bottom gate voltage ΔV_B (and equivalently in electron density of the center region K2 (n_N)). While the fan diagram is visible in negative ΔV_B , the device shows an unusually sharp magneto resistance rise around B_C = 4.5 T at positive ΔV_B (dashed red box). At lower magnetic field, resonant tunneling between Landau levels on the P and N side of the PN junction occurs. A zoom in higher resolution scan with optimized color scale can be found in figure 3C. (B) Measured resistance (R), expected resistance with full equilibrium (R_e), fitting of the low field data using our analytical quantum tunneling model in semiclassical regime (R_S) and their ratio (R/R_e) as a function of magnet field sweep at ΔV_B =5V (equal carrier density for P and N region, along the double dashed line in A). (C) Magnetic length l_B and calculated incompressible strip width d_{IS} as a function of field. (D) $B < B_C$, $l_B > d_{IS}$. The system is in the semiclassical regime, where tunneling occurs only across the gate-defined ν=0 tunnel barrier, agreeing with R_S. (E) $B > B_C$, $l_B < d_{IS}$. Incompressible strips becomes well-defined due to reduced coupling between them. Cascade tunneling occurs across all ISs, resulting in a steep double exponential increase in R and R/R_e, a deviation from semiclassical description (R_S).

state leads to:

$$\frac{4e^2}{h} dV_{\mathrm{N}}(y) = - [\gamma_{\mathrm{N}}(V_{\mathrm{N}+1}(y) - V_{\mathrm{N}}(y)) - \gamma_{\mathrm{N}-1}(V_{\mathrm{N}}(y) - V_{\mathrm{N}-1}(y))]dy \quad (1)$$

, where γ_{N} is the tunneling conductance per length between QH edge states (see SI). This equation serves as our master equation to describe the observed data.

In the low magnetic field limit $l_B > d_{IS}$, and strong tunnel coupling between the CS regions effectively smears out the delineation between IS/CS within each doped region. This leaves the tunneling across the region to dominate, and the overall tunneling barrier takes on a finite value γ_0. As a result, each N and P region behaves as one compressible state with filling factors ν' and ν. In this limit, Eq. (1) can be solved analytically (see SI Section 2) and leads to a simple expression:

$$R = \frac{V_1^P(0)}{I_0} = \frac{h}{e^2}[-\frac{2}{\nu}\frac{1}{1-exp(-\alpha L)} + \frac{1}{\nu'}\frac{1+exp(-\alpha L)}{1-exp(-\alpha L)}], \quad (2)$$

where

$$\alpha \equiv \frac{\gamma_0(\nu' - \nu)}{\nu' \nu}\frac{h}{e^2} \quad (3)$$

, and L is the length of the PN boundary. Note that this solution correctly reproduces the fully-equilibrated case at the large tunnel coupling limit where $exp(-\alpha L)$ vanishes. By fitting this model (see Supplementary Eq (11)) to the data, we obtained $\gamma_0 \approx 500\Omega^{-1}m^{-1}$, which is consistent with our experimental parameters.

As B approaches B_C, the tunnel coupling between neighboring CSs becomes weaker and the transport across the device occurs via a cascade of tunneling across the series of ISs (see SI) with incrementally changing chemical potentials (Fig. 2E). This can only be realized in wide and uniform ISs enabled by the thick hBN dielectric employed in our device in contrast to previously reported devices [21]. The crossover between semiclassical to quantum transport regime occurs when $l_B = d_{IS}$. Marked by a sharp change of the magneto resistance scaling law, this phase transition point can be utilized to accurately determine the incompressible strip width d_{IS}. In addition, this confirms that the IS becomes insulating with finite-width incompressible region only when $l_B > d_{IS}$, and the tunneling measurement accurately probes the compressibility of the participating ISs. From the electrostatic profile of the PN junction, we estimate $B_C \approx 4.5$ T (See SI), in accordance with our experimental observation. When $B > B_C$, Eq (1) leads to an additional exponential dependence of R on B on top of the trivial contribution from the ν=0 gap development (See SI). We use this additional exponential growth of R to characterize the profile of IS regions (Supplementary Fig. S3).

We now discuss oscillatory features we observe when $B < B_C$ and $l_B > d_{IS}$. The only appreciable tunneling across the PN boundary occurs through the ν= 0 region between ISs of the doped regions. In our device, we can achieve full experimental control of the energy alignment of the Fermi level, P-LLs, and N-LLs by varying the magnetic field and ΔV_B. The magnetic field causes the

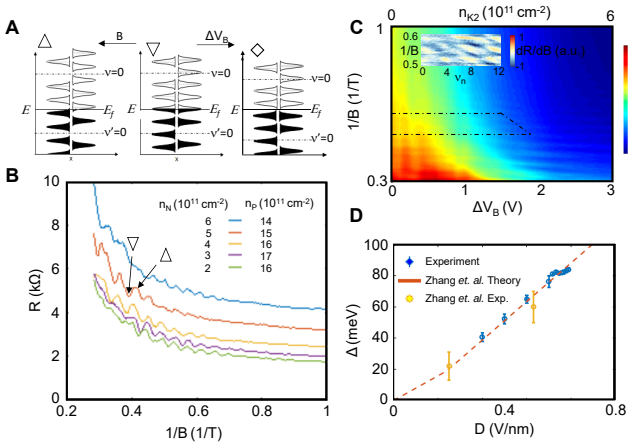

Figure 3. (Color online) Resonant Landau Tunneling in Semiclassical regime ($B < B_C$). (A) When sweeping B, Landau level alignment changes from resonance (down-triangle) to off-resonance (up-triangle), resulting in oscillations of the measured resistance R periodically with inverse magnetic field 1/B. When sweeping ΔV_B, while Landau levels are in resonance, the Fermi level can be temporarily unpinned and jump across the Landau gap (diamond), resulting into modulations of oscillation amplitude. (B) R as a periodic function of 1/B at different electron densities in the center region K2 (n_N) and hole density in region region K1 and K3 (n_P) (C) 2D scan of the resonant tunneling features verifying that the Landau level alignments are only sensitive to the PN junction height instead of individual carrier densities in each respective region. (Inset) Differentiated data in the range of the dashed region, a modulation in oscillation amplitude has been observed with a periodicity of the electron filling factor ν_n=4. (D) By tracing the peak positions as a function of field and gate voltage, we extract the spectroscopy bandgap of bilayer graphene as a function of displacement field D.

two sets of LLs to move in opposite directions in energy, resulting in oscillation of measured resistance R periodically with inverse magnetic field 1/B (fig. 3A). To ensure the energy alignment is only determined by these two experimental parameters, we conducted the tunneling measurements near zero DC bias with a small effective AC excitation in this regime. A large finite bias voltage comparable to QH gaps could unnecessarily complicate the energy alignment of Landau levels on P and N sides due to a significant chemical potential drop across the PN junction, and potentially suppress the oscillation amplitude when non-resonant breakdown current across the IS starts to dominate the transport.

The LL filling fraction of each doped region is given by $\nu_{N,P} = hn_{N,P}/eB$, where $n_{N,P}$ are the electron and hole densities in the N- (K2) and P- (K1, K3) regions, respectively. DOS is periodic in $1/B_F$, where $B_F = h(n_N + n_P)/e$ is determined only by the PN junction barrier height and not by any region-specific carrier density. We have deliberately designed the experiment so that the carrier densities in K1, K2 and K3 are simultaneously controlled by ΔV_B, so that $n_N + n_P$ stays constant in the scan, thus keeping the oscillation periodicity unchanged (Fig. 3A). Fig. 3B shows R as a function of 1/B for several different fixed gate voltages (different n_N and n_P values). We observe that the oscillation in R is clearly periodical in 1/B. From the periodicity observed in Fig. 3B, we estimated $n_N + n_P = 2 \text{ x } 10^{12} cm^{-2}$, in good agreement with the density of carriers calculated from ΔV_B and the bottom gate capacitance, confirming the oscillation is due to resonant tunneling between Landau levels instead of universal conductance fluctuation (UCF). The effective energy difference between the resonant tunneling peaks also corresponds to the Landau level splitting. In the field range plotted in Fig.3, this energy gap is much larger than the expected charging energy when treating the central region as an effective quantum dot (1μm x 1μm), and is proportional to the magnetic field B unlike the charging energy. We deliberately designed each region to be sufficient large (1μm) to avoid complication by Coulomb blockade (CB), in contrast to the small length scale necessary for relatively smaller quantum Hall systems where the UCF and CB effects become appreciable [25, 26].

In Fig 3C, we display a map of R as a function of both ΔV_B and $1/B$. Here, the oscillation in R appears as horizontal streaks but with a slight downward tilt as ΔV_B increases. The lowering of the peak with ΔV_B is due to the decreasing $\nu = 0$ tunneling barrier as the displacement-induced BLG band gap decreases. From the observed slope $\partial B/\partial V_B$ of the resonant tunneling peaks, we can estimate the bandgap Δ using $\partial\Delta/\partial V_B = \hbar e(m_e^{-1} + m_h^{-1})\partial B/\partial V_B$, where $m_{(e,h)}$ are the electron and hole effective masses in BLG, respectively. Fig. 3D shows experimentally obtained Δ as a function of displacement field $D = \varepsilon(V_T - V_B)/d_{hBN}$, where $d_{hBN} = 180$ nm is the thickness of the hBN layer, ϵ is the dielectric constant of hBN, and V_T (V_B) are the local top (bottom) gate voltages. These values are in accordance with previously obtained values [10], but with much higher energy resolution of ~ 0.1 meV.

While keeping the energy alignment of P- LLs and N-LLs constant with respect to each other, sweeping ΔV_B along the resonant tunneling peaks adjusts the Fermi level alignment, which should also yield oscillations in resistance. To demonstrate this, we plot in the inset of Fig. 3C the first derivative of the measured resistance dR/dB in the scan range denoted by the black dashed box in Fig. 3C. Along the resonance lines, we observe that dR/dB oscillates with a periodicity of $\Delta\nu_n = 4$, which is precisely the LL degeneracy in the low magnetic field limit. This agreement confirms that our spectroscopic transport technique can probe in detail the properties of LLs. Further development in the spatial engineering of QH edge state will allow us to explore emergent phenomena, such as the recently discovered quasiparticle interference

[27, 28], using the spectroscopic tunneling transport technique we demonstrate in this work. In contrast to conventional QH transport along the QH edge states, our tunneling measurement is sensitive to both the localized and extended states, and therefore allows us to probe the full density of states and the energy profile of QH states (see SI). The capability of measuring all relevant physical properties sensitively within a single device provides a powerful tool in studying QH physics to address the key remaining questions. The capability to electrostatically define, separate and guide the QH edge states can also lead to quantum interferometers to braid exotic quasiparticles in QH states.

ACKNOWLEDGEMENTS

We thank Boris Shklovskii, Amir Yacoby, Bertrand Halperin, Tony Low and Roberto Grassi for helpful discussions. The major experimental work at Harvard University is supported by the U.S. Department of Energy (grant DE-SC0012260). K.W. is supported by Army Research Office (ARO) Multidisciplinary University Research Initiative (MURI) (grant W911NF-14-1-0247). P.K. acknowledges partial support from the Gordon and Betty Moore Foundations EPiQS Initiative (grant GBMF4543). K.W. and T.T. acknowledge support from the Elemental Strategy Initiative conducted by the Ministry of Education, Culture, Sports, Science and Technology, Japan. T.T. acknowledges support from a Grant-in-Aid for Scientific Research (grant 262480621) and a grant on Innovative Areas Nano Informatics (grant 25106006) from the Japan Society for the Promotion of Science. This work was performed, in part, at the Center for Nanoscale Systems (CNS), a member of the National Nanotechnology Infrastructure Network, which is supported by the NSF under award no. ECS-0335765. CNS is part of Harvard University. A part of device fabrication was done in Albany NanoTech Institute supported by the Semiconductor Research Corporations NRI Center for Institute for Nanoelectronics Discovery and Exploration (INDEX).

[1] K. V. Klitzing, G. Dorda, and M. Pepper, Phys. Rev. Lett. **45**, 494 (1980).
[2] D. C. Tsui, H. L. Stormer, and A. C. Gossard, Phys. Rev. Lett. **48**, 1559 (1982).
[3] P. Maher, L. Wang, Y. Gao, C. Forsythe, T. Taniguchi, K. Watanabe, D. Abanin, Z. Papic, and P. K. C. R. D. P. Cadden-Zimansky, J. Hone, Science **345**, 61 (2014).
[4] C. R. Dean, L. Wang, P. Maher, C. Forsythe, F. Ghahari, Y. Gao, J. Katoch, M. Ishigami, P. Moon, M. Koshino, T. Taniguchi, K. Watanabe, K. L. Shepard, J. Hone, and P. Kim, Nature **497**, 598 (2013).
[5] M. Dolev, M. Heiblum, V. Umansky, A. Stern, and D. Mahalu, Nature **452**, 829 (2008).
[6] E. M. Spanton, A. A. Zibrov, H. Zhou, T. Taniguchi, K. Watanabe, M. P. Zaletel, and A. F. Young., Science **10**, 1126 (2018).
[7] C. Nayak, S. H. Simon, A. Stern, M. Freedman, and S. D. Sarma, Rev. Mod. Phys **80**, 1083 (2008).
[8] J. Martin, B. E. Feldman, R. T. Weitz, M. T. Allen, and A. Yacoby, Phys. Rev. Lett **105**, 256806 (2010).
[9] J. Martin, N. Akerman, G. Ulbricht, T. Lohmann, K. von Klitzing, J. H. Smet, and A. Yacoby, Nature Physics **5**, 669 (2009).
[10] Y. Zhang, T.-T. Tang, C. Girit, Z. Hao, M. C. Martin, A. Zettl, M. F. Crommie, Y. Shen, and F. Wang, Nature **459**, 820 (2009).
[11] A. F. Young and L. S. Levitov, Phys. Rev. B **84**, 085441 (2011).
[12] N. Pascher, C. Rssler, T. Ihn, K. Ensslin, C. Reichl, and W. Wegscheider, Phys. Rev. X **4**, 011014 (2014).
[13] M. E. Suddards, A. Baumgartner, M. Henini, and C. J. Mellor, New J. Phys. **14**, 083015 (2012).
[14] D. B. Chklovskii, B. I. Shklovskii, and L. I. Glazman, Phys. Rev. B **46**, 4026 (1992).
[15] J. C. Y. Teo and C. L. Kane, Phys. Rev. B **89**, 085101 (2014).
[16] G. Binnig and H. Rohrer, IBM Journal of Research and Development **30**, 355 (1986).
[17] F. Martins, S. Faniel, B. Rosenow, H. Sellier, S. Huant, M. G. Pala, L. Bayot, X. Wallart, V. Bayot, and B. Hackens, Scientific Reports **3**, 1416 (2013).
[18] L. Wang, I. Meric, P. Y. Huang, Q. Gao, Y. Gao, H. Tran, T. Taniguchi, K. Watanabe, L. M. Campos, D. A. Muller, J. Guo, P. Kim, J. Hone, K. L. Shepard, and C. R. Dean, Science **1**, 342 (2013).
[19] R. V. Gorbachev, J. C. W. Song, G. L. Yu, A. V. Kretinin, F. Withers, Y. Cao, A. Mishchenko, I. V. Grigorieva, K. S. Novoselov, L. S. Levitov, and A. K. Geim, Science **346**, 448 (2014).
[20] S. Morikawa, M. S., R. Moriya, K. Watanabe, T. Taniguchi, and T. Machida, Appl. Phys. Lett. **106**, 183101 (2015).
[21] D. S. Wei, T. van der Sar, J. D. Sanchez-Yamagishi, K. Watanabe, T. Taniguchi, P. Jarillo-Herrero, B. I. Halperin, and A. Yacoby, Science Advances **3**, e1700600 (2017).
[22] B. zyilmaz, P. Jarillo-Herrero, D. Efetova, D. A. Abanin, L. S. Levitov, and P. Kim, Phys. Rev. Lett. **99**, 166804 (2017).
[23] J. R. Williams, L. DiCarlo, and C. M. Marcus, Science **317**, 638 (2007).
[24] F. Amet, J. R. Williams, K. Watanabe, and T. T. D. Goldhaber-Gordon, Phys. Rev. Lett. **112**, 196601 (2014).
[25] D. H. Cobden, M. Bockrath, P. L. McEuen, A. G. Rinzler, and R. E. Smalley, Phys. Rev. Lett. **81**, 681 (1998).
[26] M. Eich, R. Pisoni, H. Overweg, A. Kurzmann, Y. Lee, P. Rickhaus, T. Ihn, K. Ensslin, F. Herman, M. Sigrist, K. Watanabe, and T. Taniguchi, Phys. Rev. X 8, 031023 **8**, 031023 (2018).
[27] I. Neder, N. Ofek, Y. Chung, M. Heiblum, D. Mahalu, and V. Umansky, Nature **448**, 333 (2007).
[28] Y. Ji, Y. Chung, D. Sprinzak, M. Heiblum, D. Mahalu, and H. Shtrikman, Nature **422**, 415 (2003).